Switched 4-to-1 Transimpedance Combining Amplifier for Receiver Front-End Circuit of Static Unitary Detector-Based LADAR System

Eun-Gyu Lee [1], Jae-Eun Lee [1], Bang Chul Jung [1], Bongki Mheen [2] and Choul-Young Kim [1,*] ID

[1]   Department of Electronics Engineering, Chungnam Nation University, Daejeon 34134, Korea; eungyu@cnu.ac.kr (E.-G.L.); yje1128@cnu.ac.kr (J.-E.L.); bcjung@cnu.ac.kr (B.C.J.)
[2]   Electronics and Telecommunication Research Institute, Daejeon 34134, Korea; bkmheen@etri.re.kr
*   Correspondence: cykim@cnu.ac.kr; Tel.: +82-42-821-5663

Abstract: Laser detection and ranging (LADAR) systems are commonly used to acquire real-time three-dimensional (3D) images using the time-of-flight of a short laser pulse. A static unitary detector (STUD)-based LADAR system is a simple method for obtaining real-time high-resolution 3D images. In this study, a switched 4-to-1 transimpedance combining amplifier (TCA) is implemented as a receiver front-end readout integrated circuit for the STUD-based LADAR system. The 4-to-1 TCA is fabricated using a standard 0.18 μm complementary metal-oxide-semiconductor (CMOS) technology, and it consists of four independent current buffers, a two-stage signal combiner, a balun, and an output buffer in one single integrated chip. In addition, there is a switch on each input current path to expand the region of interest with multiple photodetectors. The core of the TCA occupies an area of 92 μm × 68 μm, and the die size including I/O pads is 1000 μm × 840 μm. The power consumption of the fabricated chip is 17.8 mW for a supplied voltage of 1.8 V and a transimpedance gain of 67.5 dBΩ. The simulated bandwidth is 353 MHz in the presence of a 1 pF photodiode parasitic capacitance for each photosensitive cell.

Keywords: LADAR; STUD; switched-TCA; optical receiver

1. Introduction

Laser detection and ranging (LADAR) systems are commonly used to acquire real-time three-dimensional (3D) images using the time-of-flight (TOF) of a short laser pulse. As LADAR technology has become more diverse, it has been utilized in various applications, such as autonomous vehicles, robots, remote sensing, reconnaissance, and motion detection, where high 3D resolution is important [1–10]. For the real-time acquisition of 3D images, a LADAR system must process all reflected TOF laser signals from every direction for a region-of-interest (ROI) in real time.

There are different methods of implementing LADAR systems. The static unitary detector (STUD)-based technique [11] has some unique advantages compared with other techniques, such as the rotational motion-based technique [12] or the focal plane array (FPA)-based technique [13]. Because the STUD-based technique has only one signal processing chain and does not need micro-lenses to increase the signal-to-noise ratio (SNR), it is cost effective. In addition, the required power level of the transmitted laser pulse is not as high as for the FPA-based technique because the STUD-based technique illuminates one collimated laser pulse at a time in a specific direction. Figure 1 shows the block diagram of a STUD-based LADAR system. In the STUD-based LADAR system, the transmitter emits laser pulses over the entire ROI with two high-speed optical scanners and the receiver detects the returned optical pulses to a static-unitary large-area photodetector.
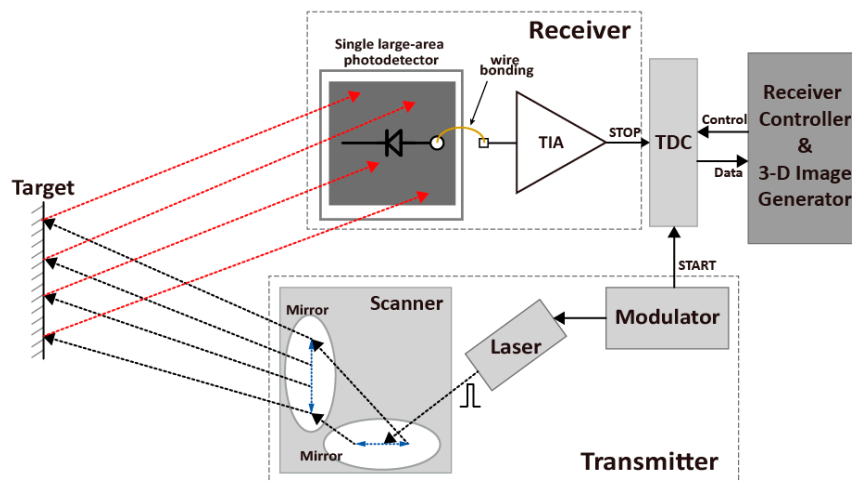
Figure 1. Block diagram of the static unitary detector (STUD)-based laser detection and ranging (LADAR) system.

However, an increase in the area of the photodetector results in a decrease in the bandwidth of the receiver due to the large parasitic capacitance of the large-area photodetector. To overcome this problem, the STUD-based LADAR receiver has multiple partitioned photosensitive cells, as shown in Figure 2. Each of the partitioned cells has its own transimpedance amplifier (TIA) to receive and amplify the optical current from each partitioned cell independently, and then a signal combiner sums all the outputs of each TIA into a single output signal STOP, which indicates the arrival of the return signal. A time-to-digital converter (TDC) calculates the TOF between the START and STOP signals. Since each partitioned cell with its own cascading TIA operates independently without affecting any of the other cells, its bandwidth remains unchanged. In addition, since the STUD-based LADAR receiver does not need to determine which cell detects the arriving laser pulse, inter-channel-interference is not a problem, unlike in the FPA-based LADAR receiver.
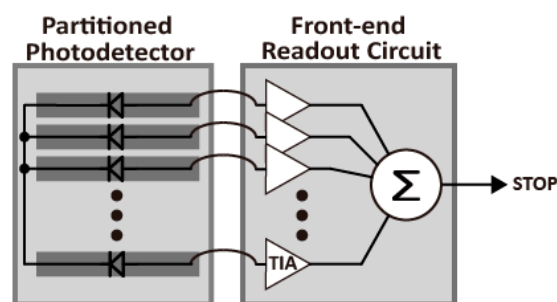

Figure 2. STUD-based LADAR receiver with partitioned photodetector.

To implement a STUD-based LADAR receiver, the same number of TIAs as partitioned photosensitive cells is needed, and they are assembled on a single board. The pad pitch in the partitioned photodetector is totally different from the pad interval of the TIAs. In case the lengths of the interconnection lines between each photosensitive cell and the corresponding TIA is different, accurate time information cannot be obtained because the time delay varies depending on which photosensitive cell receives the return signal. Therefore, the electrical length of the interconnection lines between each photosensitive cell and the corresponding TIA should be designed equal on the test fixture. This limits the number of cells for higher-resolution 3D images over a large ROI due to the interconnection problem between a partitioned photodetector and multiple TIAs [14,15]. To resolve this problem, a 4-to-1 transimpedance combining amplifier (TCA) was proposed in our previous work [14] as the

front-end readout integrated circuit (ROIC) for the STUD-based LADAR receiver with a photodetector, which has four photosensitive partitioned cells.

In this study, we propose a switched 4-to-1 TCA. The switched 4-to-1 TCA has a switch on each input current path, as shown in Figure 3. The photodetector in this work has four photosensitive cells. The target size of a single photosensitive cell is 350 μm × 100 μm and the parasitic capacitance of the single cell is assumed to be 1 pF. In the STUD-based LADAR receiver, it is necessary to increase the photosensitive area of the photodetector in order to enlarge the ROI in the STUD-based LADAR receiver. Meanwhile, this increases the noise of the receiver due to the large-area photodetector. The proposed switched 4-to-1 TCA can be used, as shown in Figure 4, in the STUD-based LADAR receiver front-end. According to the position where the returned laser pulse arrives, one of the TCAs is switched on to receive the optical current and the others are not connected to the photodetector. Therefore, the noise generated from the unconnected photodetector cannot affect the receiver. The switch control signal *EN* causes the switch to be turned on. Depending on the ROI, it is predicted which photodetector will detect the return signal, so that the *EN* signal is able to turn on the corresponding switch.
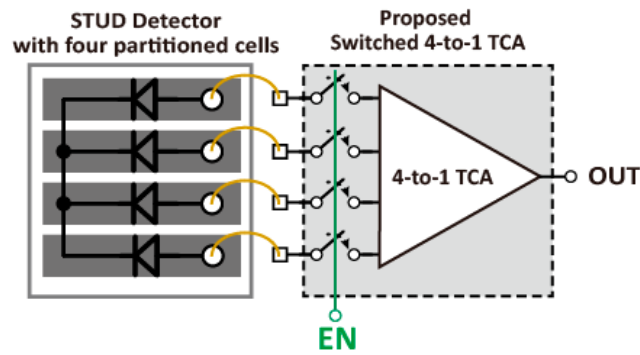

Figure 3. Proposed switched 4-to-1 transimpedance combining amplifier (TCA) with four partitioned photodetectors.
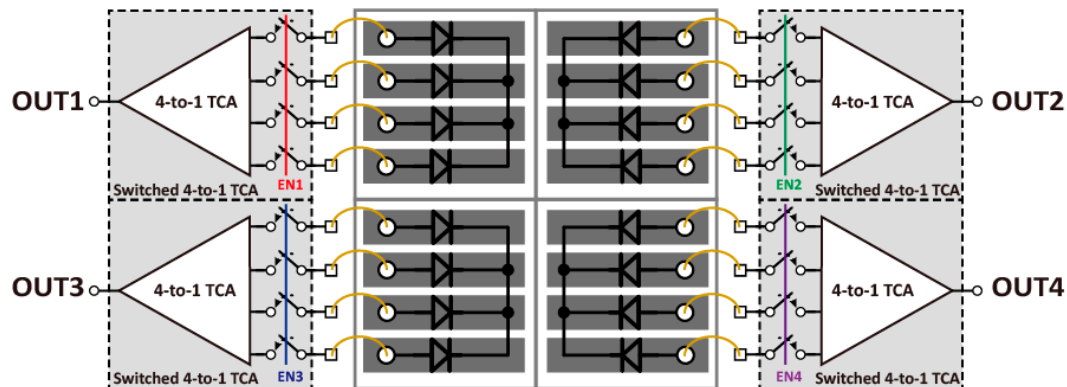

Figure 4. Operation example with the four proposed switched 4-to-1 TCAs and four multiple partitioned photodetectors.

The TCA amplifies and combines current signals generated using the photosensitive cells from incoming optical signals into one voltage signal for further processing. The switched 4-to-1 TCA is fabricated using a standard complementary metal-oxide-semiconductor (CMOS) 0.18 μm technology. It provides 3.8 pA/$\sqrt{\text{Hz}}$ average noise current spectral density with a bandwidth of 353 MHz and a transimpedance gain of 67.5 dBΩ. The core of the TCA consumes 17.8 mW of power from a 1.8 V supply. The core of the TCA occupies an active area of about 92 μm × 68 μm and the die size including I/O pads is 1000 μm × 840 μm.

2. Architecture Description

The block diagram of the proposed switched 4-to-1 TCA is shown in Figure 5. It amplifies and combines the photocurrent from the four partitioned photosensitive cells into one voltage signal. The switched 4-to-1 TCA consists of four primary stages: (1) four over-current protection (OCP) circuits; (2) four switches, four current buffers; (3) a signal combiner; and (4) a post-amplifier. The OCP circuits prevent the fabricated chip from being damaged by a very high input signal. The switch is turned on when the reflected laser pulse arrives at the corresponding photodetector among the multiple detectors. The current buffer is a low impedance input stage intended to receive the optical current from a photosensitive cell. The signal combiner sums the outputs of all the current buffers. The post-amplifier is designed to preserve the bandwidth and to enhance the transimpedance gain. A balun is a differential amplifier with differential input signals biased at the same direct current (DC) level to convert the single-ended output of the signal combiner into a differential signal. The output buffer is a differential amplifier with resistor loads of 50 Ω on both the positive and negative outputs. The schematic diagram of the designed circuit is illustrated in Figure 6.
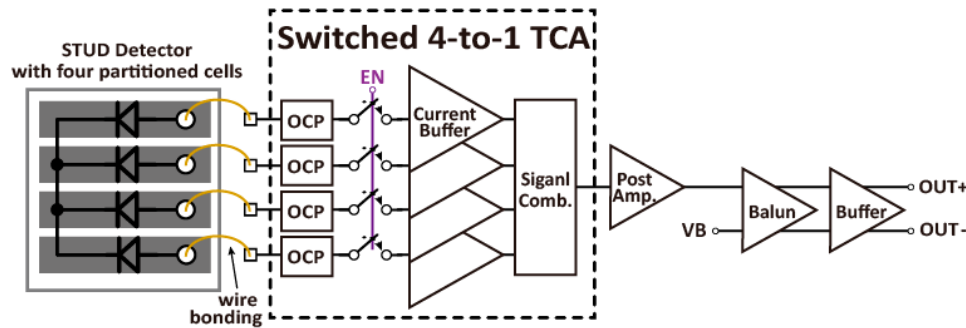

Figure 5. Block diagram of the proposed switched 4-to-1 TCA with a balun and an output buffer.
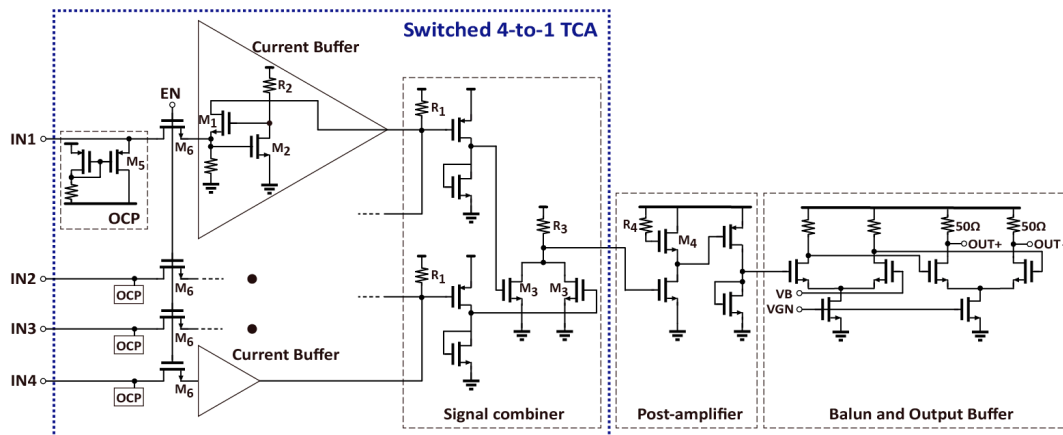

Figure 6. Schematic diagram of the proposed switched 4-to-1 TCA.

2.1. OCP and Input Switch

The OCP circuit, as shown in Figure 6, is designed to protect the 4-to-1 TCA from being damaged by a very high input current [16]. The transistor M_5 turns on when its source voltage is larger than 1.04 V. As shown in Figure 7, when the input current is approximately 400 μA, the source voltage of M_5 reaches 1.043 V. When the input current is larger than 400 μA, the increase in the input voltage is suppressed and the sink current to the OCP circuit increases. Therefore, the effective range of the input voltage is from the DC bias voltage of the input current buffer, approximately 610 mV to 1.043 V, before the OCP circuit turns on.

To expand the ROI with multiple partitioned photodetectors, a switch is added on each input current path. Several types of switches, such as n-channel metal-oxide-semiconductor field effect transistor (NMOSFET or NMOS), p-channel MOSFET (PMOSFET or PMOS), and CMOS transmission gates, are available. In this study, NMOS switches M_6 are used on all input current paths, as shown in Figure 6. A high output will be degraded by the NMOS switch, since the NMOS switch turns off when the input becomes $EN - V_{th}$, where EN is a control signal of the switch and V_{th} is the threshold voltage of the switch transistor M_6. The maximum input value of the NMOS switch without signal degradation is approximately 1.175 V when the V_{th} of M_6 is about 625 mV, and the available maximum input voltage dependent on the input photocurrent is 1.043 V. Therefore, an NMOS switch on the input path is capable of passing an input signal having a value from 610 mV to 1.043 V. A PMOS switch is not a viable solution, since the threshold voltage is larger than 610 mV and a low input signal cannot be passed through a PMOS switch.
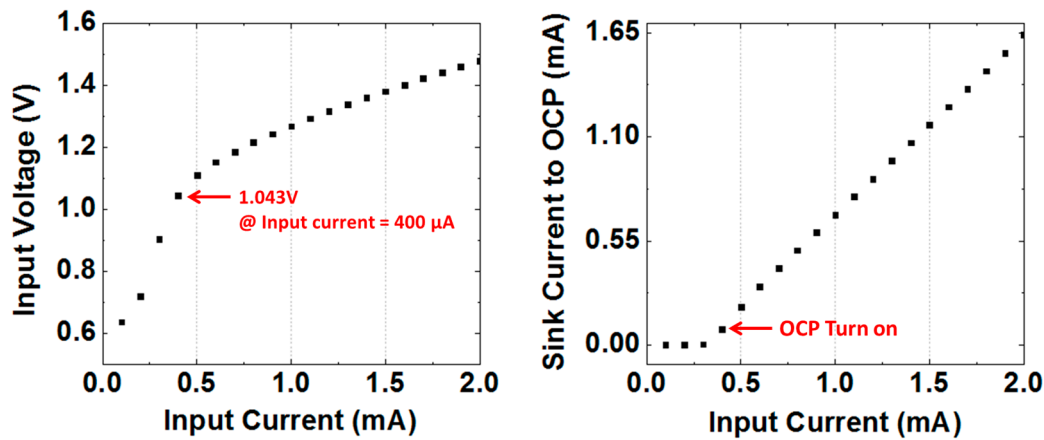

Figure 7. Simulated input voltage and sink current to OCP (over-current protection) circuit according to the input current.

2.2. 4-to-1 TCA, Post-Amplifier, Balun, and Output Buffer

Four copies of the regulated cascode (RGC) topology are selected as current buffers because of their low input impedance and wide bandwidth characteristics, as compared to other topologies such as the inverter, common-source, and common-gate topologies [17]. The RGC structure reduces the input impedance significantly by using the M_2 and R_2 stage as a local feedback to boost the transconductance of M_1. The small-signal impedance of the RGC structure (Z_{in}) is given by (1):

$$Z_{in} \cong \frac{1}{g_{m1}(1 + g_{m2}R_2)},$$
(1)

where g_{m1} and g_{m2} are the transconductances of M_1 and M_2, respectively.

The signals from the current buffers combine through two stages, as shown in Figure 6. In the first stage, two inputs are summed through the output load resistor R_1 of the RGC TIA. In the second stage, common-source amplifiers are used at the outputs of the two first-combining stages, and their currents are summed through a single resistive load R_3. There is a common-source amplifier between the first and second combining stages that functions as a buffer and a bias shifter.

To analyze the effect of the noise introduced by partitioned photosensitive cells and the TCA, the simplified circuit is illustrated in Figure 8 with noise factors [15]. The equivalent total input referred noise of the TCA is approximately given by (2):

$$\overline{i_{n,in}^2} \cong \frac{\overline{v_{n,OUT}^2}}{Z_{T,TCA}} = 4\left\{\left(\overline{i_{n,PD}^2} + \overline{i_{n,CB}^2}\right) + \frac{\overline{i_{n,R1}^2}}{2}\right\} \cdot R_1 + \frac{\left(2\overline{i_{n,C2}^2} + \overline{i_{n,R3}^2}\right) \cdot R_3^2}{Z_{T,TCA}}$$
(2)

where $\overline{i_{n,PD}^2}$ is the noise from a single photosensitive cell, $\overline{i_{n,CB}^2}$ is the generated noise in the current buffer stage, $\overline{i_{n,C2}^2}$ is the generated noise in the second combining stage, and $\overline{i_{n,R1}^2}$ and $\overline{i_{n,R3}^2}$ are the thermal noise from R_1 and R_3, respectively. In this analysis, we assume that:

$$\overline{i_{n,PD}^2} = \overline{i_{n,PD1}^2} = \overline{i_{n,PD2}^2} = \overline{i_{n,PD3}^2} = \overline{i_{n,PD4}^2}$$

$$\overline{i_{n,CB}^2} = \overline{i_{n,CB1}^2} = \overline{i_{n,CB2}^2} = \overline{i_{n,CB3}^2} = \overline{i_{n,CB4}^2}$$

$$\overline{v_{n,C1}^2} = \overline{v_{n,C1,1}^2} = \overline{v_{n,C1,2}^2}$$

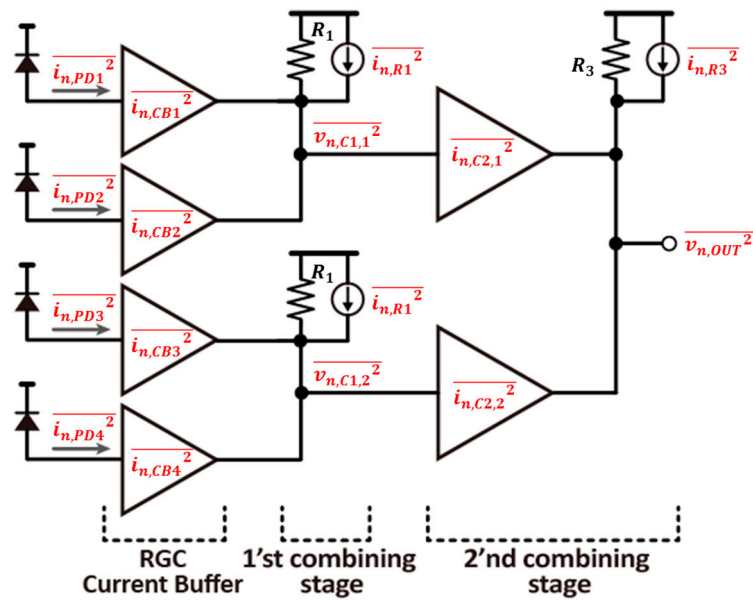$$\overline{i_{n,C2}^2} = \overline{i_{n,C2,1}^2} = \overline{i_{n,C2,2}^2}.$$

Figure 8. Simplified circuit for noise analysis.

In (2), the receiver noise with a large-area photodetector, even though it is partitioned, is increased in the developed TCA. The noise generated in the first combining stage with the current buffer is also the dominant factor of the equivalent total noise.

The post-amplifier is realized using a two-stage common-source amplifier. The first stage has an active inductor load, consisting of a transistor M_4 and a resistor R_4, to increase the overall bandwidth [18]. The second stage controls the pulse polarity and the DC bias.

The balun converts the single-ended TCA output signal to differential signals. The balun and output buffer are illustrated in Figure 6. The balun is a differential amplifier with differential inputs biased at the same DC level. In this study, the same DC voltage as compared with the output voltage of the TCA is applied through additional DC bias port *VB*. The output buffer is also a differential amplifier, and it is designed to match the output impedances to 50 Ω on both the positive and negative outputs.

The full width at half maximum (FWHM) of the input pulse used in this work is about 2.2 ns and its rise time is ~1 ns. The bandwidth required for the designed TCA to preserve its rise time is approximated by [19,20] as:

$$BW \cong \frac{0.35}{t_r}, \tag{3}$$

where t_r is the rise time of the input pulse. For a rise time of 1 ns, (3) gives a bandwidth of approximately 350 MHz. The simulated transimpedance gain of the developed TCA obtained using this balun and output buffer is shown in Figure 9. The transimpedance gain is approximately 68 dBΩ and the -3 dB

frequency is approximately 353 MHz with a photodetector parasitic capacitance of 1 pF. The gain and bandwidth from each circuit stage is summarized in Table 1.
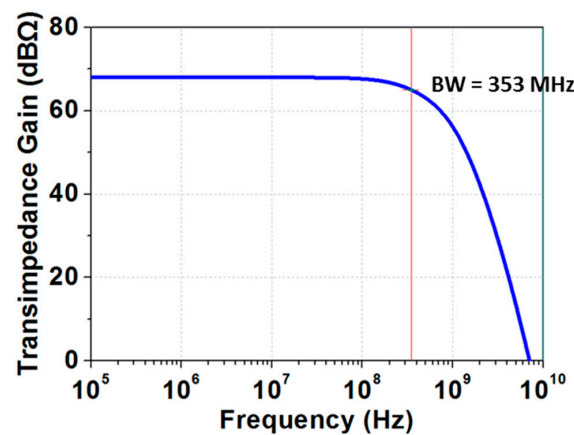

Figure 9. Simulated transimpedance gain of the proposed TCA obtained using this balun and output buffer.

Table 1. Summary of the circuit designed performances.

Stage	Gain	Bandwidth	Direct Current (DC)
Current buffers and first combining stages (R_1)	70 dBΩ (3 kΩ)	330 MHz	1.48 mA
Second combining stage	2 dB	310 MHz	0.65 mA
Post-amplifier	6 dB	415 MHz	2.06 mA
Balun and output buffer	−10 dB	353 MHz	3.78 mA

3. Measurement Results

The switched 4-to-1 TCA was implemented in a 0.18 μm CMOS technology. The core occupies an area of 92 μm × 68 μm, and the die size including I/O pads is 1000 μm × 840 μm. A microphotograph of the fabricated chip with bond wires on the test fixture is shown in Figure 10. All the biases were applied through bond wires, and short pulse response measurement was performed with a coaxial micro-receptacle (CMJ) connector.
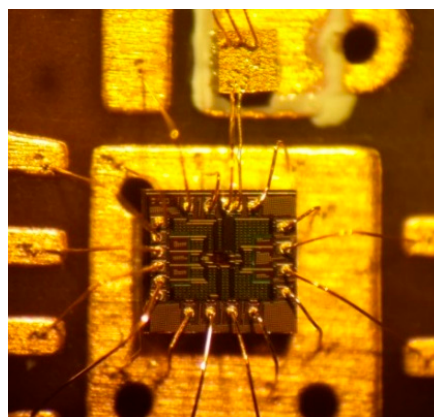

Figure 10. Microphotograph of the fabricated chip with bond wires on the test fixture.

The fabricated chip was mounted on a wire-bonded chip-on-board (COB) module to measure the electrical pulse response, as shown in Figure 11a. A 10-kΩ resistor acts as a voltage-to-current converter. To measure the pulse transient response of the fabricated circuit, an electrical pulse signal,

generated from an Agilent 81110A pattern generator (Keysight, Santa Clara, CA, USA), was applied to each input channel of the implemented test fixture, as shown in Figure 11b. The OUT+ and OUT− signals were measured using an Agilent DSO7104B oscilloscope.
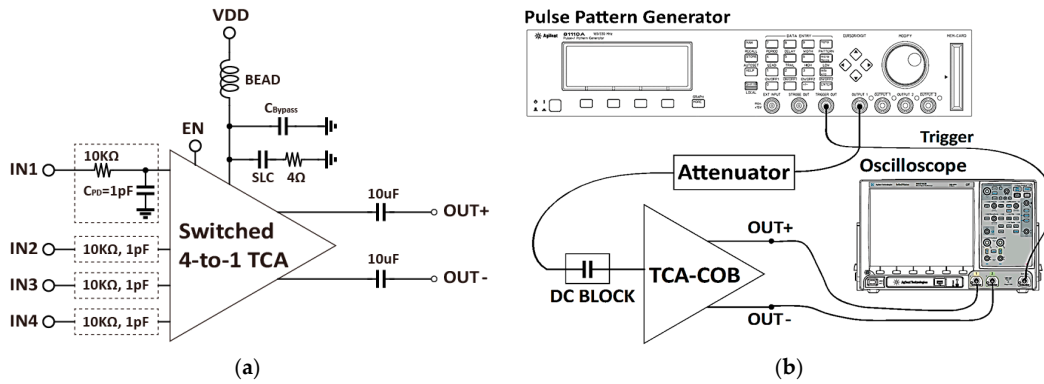

Figure 11. (**a**) TCA-chip on board (COB) schematic for electrical pulse response; (**b**) measurement setup for electrical pulse response.

Figure 12 shows the measured transient pulse response for the fabricated chip. The pulse magnitude of the input voltage from the pattern generator is adjusted so that the input current becomes 20 μA and the FWHM of the input signal is 2.2 ns with a 1.8 ns rise time, which is the minimum rise time of the Agilent 81110A pattern generator. The input current is applied to each successive input channel from IN1 through IN4, and 200 segment pulse responses of OUT+ and OUT− are measured. The blue lines represent the pulse response of 200 segments, and the red line represents the average pulse response value. The average peak-voltage of the measured output pulses is approximately 47.4 mV, and hence, the transimpedance gain is calculated to be 67.5 dBΩ using by (4). This value is very near the simulated results of 68 dBΩ.

$$Z_T = 20 \times \log_{10}\left(\frac{47.4\ \text{mV}}{20\ \mu\text{A}}\right) \tag{4}$$
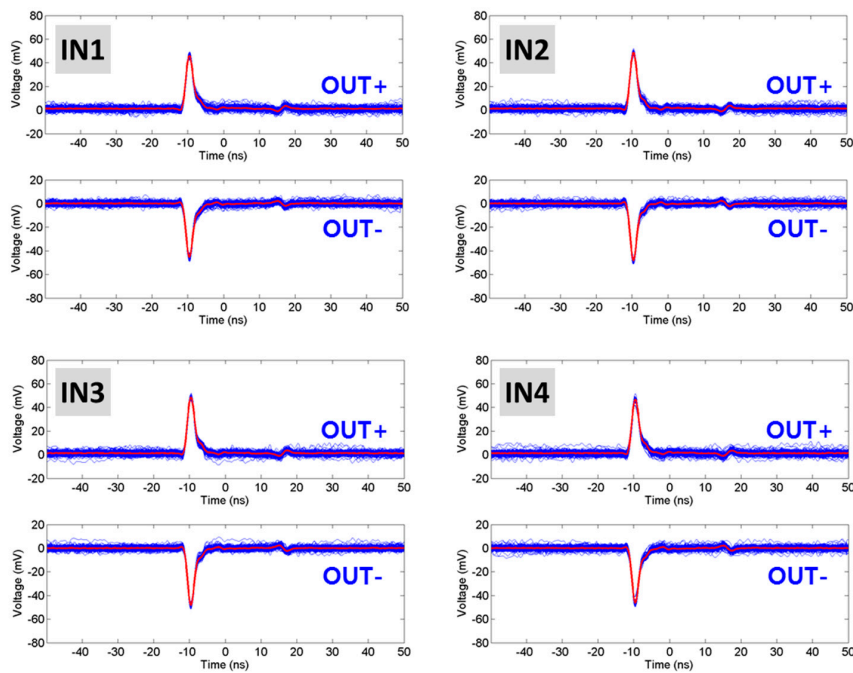

Figure 12. Measured transient pulse response for the fabricated chip.

The integrated single-ended output noise of the switched 4-to-1 TCA was measured via the oscilloscope root-mean-square (RMS) calculation function with no input signal source, as shown in Figure 13 [21]. The standard deviation of the output was measured to be 0.524 mV. After subtracting the inherent oscilloscope noise of 0.4 mV$_{rms}$, the corrected single-ended integrated output noise of the TCA was estimated to be 0.338 mV$_{rms}$. The integrated input-referred noise of the differential output of the switched 4-to-1 TCA for each input channel can be calculated as in Reference [22].

$$I_{n,in} \approx \frac{1}{4} \cdot \frac{2\sqrt{(0.524 \text{ mV})^2 - (0.4 \text{ mV})^2}}{67.5 \text{ dB}\Omega} = 0.07 \ \mu A_{rms} \tag{5}$$
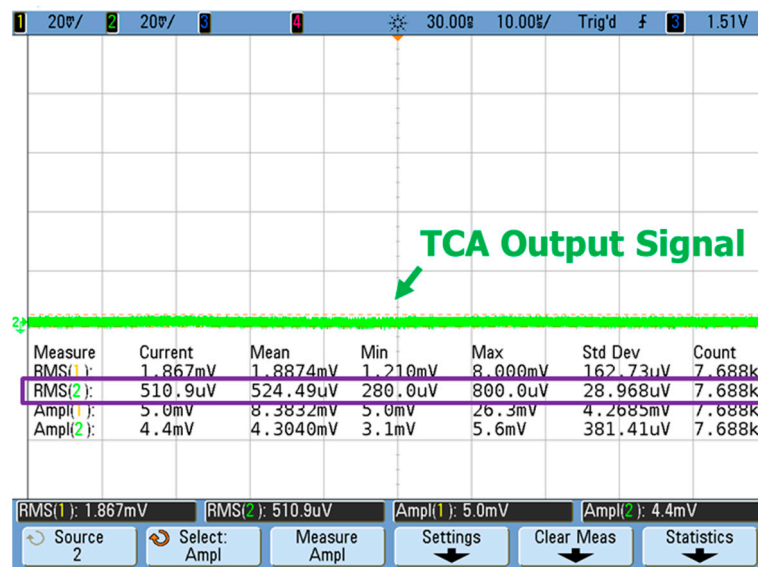

Figure 13. Integrated single-ended output noise of the switched 4-to-1 TCA.

The average input-referred noise current density is:

$$I_{n,in,avg} \approx \frac{I_{n,in}}{\sqrt{BW}} = 3.8 \text{ pA}/\sqrt{\text{Hz}} \tag{6}$$

The switched 4-to-1 TCA used a supply voltage of 1.8 V and dissipated 17.8 mW of power. The performances of the TCA are summarized in Table 2.

Table 2. Summary of the switched 4-to-1 TCA performances.

Parameter	Performance
Combining Channel	4
C_{PD}/cell (pF)	1
Effective total C_{PD} (pF)	4
Transimpedance gain (dBΩ)	67.5
Bandwidth (MHz)	353 (simulated)
Input-referred noise current density/cell (pA/$\sqrt{\text{Hz}}$)	3.8
Power consumption (mW)	17.8
Chip size (mm^2)	1.00×0.84
Technology	Complementary metal-oxide-semiconductor (CMOS) 0.18 μm

4. Conclusions

A compact switched 4-to-1 TCA was implemented using 0.18 μm CMOS technology and was used as a receiver front-end ROIC for a STUD-based LADAR system. A switch was inserted on the input path of the TCA to expand the effective photosensitive area without increasing the noise from the large-area photodetector of the STUD-based LADAR system. The space between the partitioned photosensitive cells and its cascading current buffers was made smaller by about several hundred micrometers by integrating several TIAs and a signal combiner onto a single chip. The fabricated chip had a power consumption of 17.8 mW for a 1.8 V supplied voltage, an average input-referred noise current spectral density of 3.8 pA/$\sqrt{\text{Hz}}$, and a transimpedance gain of 67.5 dBΩ. The chip was operated based on the same working principle as the STUD-based LADAR receiver. Therefore, the compact switched 4-to-1 TCA is suitable for the front-end ROIC of the STUD-based LADAR system as one integrated chip.

Author Contributions: Eun-Gyu Lee made the study design and performed the experiment, as well as the manuscript writing; Jae-Eun Lee and Bang Chul Jung contributed to the data analysis and results discussion; Bongki Mheen suggested the idea and organized the paperwork. Choul-Young Kim participated in research plan development and revised the manuscript. All authors have contributed to the manuscript.

Conflicts of Interest: The authors declare no conflict of interest.

References

1. Thrun, S.; Montemerlo, M.; Dahlkamp, H.; Stavens, D.; Aron, A.; Diebel, J.; Fong, P.; Gale, J.; Halpenny, M.; Hoffmann, G.; et al. Stanley: The robot that won the DARPA grand challenge. *J. Field Robot.* **2006**, *23*, 661–692. [CrossRef]

2. Kaisto, I.; Kostamovaara, J.; Moring, I.; Myllyla, R. Laser rangefinding techniques in sensing of 3D objects. In Proceedings of SPIE—Sensing and Reconstruction of Three-Dimensional Objects and Scenes, Santa Clara, CA, USA, 1 January 1990; SPIE: Bellingham, WA, USA, 1990; Volume 1260, pp. 122–133.

3. Hollaus, M.; Wagner, W.; Maier, B.; Schadauer, K. Airborne laser scanning of forest stem volume in a mountainous environment. *Sensors* **2007**, *7*, 1559–1577. [CrossRef]

4. Buller, G.; Wallace, A. Ranging and three-dimensional imaging using time-correlated single-photon counting and point-by-point acquisition. *IEEE J. Sel. Top. Quantum Electron.* **2007**, *13*, 1006–1015. [CrossRef]

5. Dorninger, P.; Pfeifer, N. A comprehensive automated 3D approach for building extraction, reconstruction, and regularization from airborne laser scanning point clouds. *Sensors* **2008**, *8*, 7323–7343. [CrossRef] [PubMed]

6. Wang, C.; Glenn, N.F. Integrating LIDAR intensity and elevation data for terrain characterization in a forested area. *IEEE Geosci. Remote Sens. Lett.* **2009**, *6*, 463–466. [CrossRef]

7. Amzajerdian, F.; Gao, C.-Q.; Xie, T.-Y. 3D imaging LADAR with linear array devices: Laser, detector and ROIC. In Proceedings of SPIE—International Symposium on Photoelectronic Detection and Imaging 2009: Laser Sensing and Imaging, Beijing, China, 17 June 2009; SPIE: Bellingham, WA, USA, 2009; Volume 7382, p. 738209.

8. Kurtti, S.; Kostamovaara, J. An integrated laser radar receiver channel utilizing a time-domain walk error compensation scheme. *IEEE Trans. Instrum. Meas.* **2011**, *60*, 146–157. [CrossRef]

9. Kang, Y.; Roh, C.; Suh, S.B.; Song, B. A Lidar-Based Decision-Making Method for Road Boundary Detection Using Multiple Kalman Filters. *IEEE Trans. Ind. Electron.* **2012**, *59*, 432–4368. [CrossRef]

10. Chen, J.; Zhao, P.; Liang, H.; Mei, T. Motion Planning for Autonomous vehicle Based on Radial Basis Function Neural in Unstructured Environment. *Sensors* **2014**, *14*, 17548–17566. [CrossRef] [PubMed]

11. Mheen, B.; Shim, J.-S.; Oh, M.S.; Song, J.; Song, M.; Choi, G.D.; Seo, H.; Kwon, Y.-H. High-resolution three-dimensional laser radar with static unitary detector. *Electron. Lett.* **2014**, *50*, 313–315. [CrossRef]

12. Glennie, C.; Lichti, D.D. Static calibration and analysis of the velodyne HDL-64E S2 for high accuracy mobile scanning. *Remote Sens.* **2010**, *2*, 1610–1624. [CrossRef]

13. Stettner, R.; Bailey, H.; Silverman, S. Three dimensional Flash LADAR focal planes and time dependent imaging. *Int. J. High Speed Electron. Syst.,* **2008**, *18*, 401–406. [CrossRef]

14. Lee, E.G.; An, J.; Kim, C.Y. A fully integrated four-input combining receiver front-end circuit for laser radar with static unitary detector. *Electron. Lett.* **2014**, *50*, 1543–1545. [CrossRef]

15. Lee, E.G.; Lee, J.E.; Song, M.; Choi, G.D.; Mheen, B.; Jung, B.C.; Kim, C.Y. 4-to-1 Transimpedance Combining Amplifier-Based Static Unitary Detector for High-Resolution of LADAR Sensor. *Analog Integr. Circuits Signal Process.* **2016**, submitted.

16. Ngo, T.-H.; Kim, C.-H.; Kwon, Y.J.; Ko, J.S.; Kim, D.-B.; Park, H.-H. Wideband receiver for a three-dimensional ranging LADAR system. *IEEE Trans. Circuits Syst. I Regul. Pap.* **2013**, *60*, 448–456. [CrossRef]

17. Park, S.M.; Yoo, H. 1.25-Gb/s regulated cascode CMOS transimpedance amplifier for gigabit ethernet applications. *IEEE J. Solid-State Circuits* **2004**, *39*, 112–121. [CrossRef]

18. Lee, T.H. *The Design of CMOS Radio-Frequency Integrated Circuits*, 2nd ed.; Cambridge University Press: Cambridge, UK, 2003.

19. Ziemer, R.; Tranter, W. *Principles of Communications*, 2nd ed.; Houghton Mifflin: Boston, MA, USA, 1985.

20. Ruotsalainen, T.; Palojärvi, P.; Kostamovaara, J. A wide dynamic range receiver channel for a pulsed time-of-flight laser radar. *IEEE J. Solid-State Circuits* **2001**, *36*, 1228–1238. [CrossRef]

21. Weiner, J.S.; Lee, J.S.; Leven, A.; Baeyens, Y.; Houtsma, V.; Georgiou, G.; Yang, Y.; Frackoviak, J.; Tate, A.; Reyes, R.; et al. An InGaAs-InP HBT differential transimpedance amplifier with 47-GHz bandwidth. *IEEE J. Solid-State Circuits* **2004**, *39*, 1720–1723. [CrossRef]

22. Li, C.; Palermo, S. A low-power 26-GHz transformer-based regulated cascode SiGe BiCMOS transimpedance amplifier. *IEEE J. Solid-State Circuits* **2013**, *48*, 1264–1275. [CrossRef]